# Design and Thermal Analysis of a 3D Printed Impingement Pin Fin Cold Plate for Heterogeneous Integration Application

Cong Hiep Hoang<sup>a</sup>, Arad Azizi<sup>a</sup>, Najmeh Fallahtafti<sup>a</sup>, Srikanth Rangarajan<sup>a</sup>, Vahideh Radmard<sup>a</sup>, Charles Arvin<sup>b</sup>, Kamal Sikka<sup>b</sup>, Scott Schiffres<sup>a</sup>, Bahgat Sammakia<sup>a</sup>.

<sup>a</sup> Department of Mechanical Engineering, State University of New York at Binghamton, Binghamton, NY, USA

<sup>b</sup> IBM Corporation, NY, USA

#### Abstract

Miniaturization and high heat flux of power electronic devices have posed a colossal challenge for adequate thermal management. Conventional air-cooling solutions are inadequate for high-performance electronics. Liquid cooling is an alternative solution thanks to the higher specific heat and latent heat associated with the coolants. Liquid-cooled cold plates are typically manufactured by different approaches such as: skived, forged, extrusion, electrical discharge machining. When researchers are facing challenges at creating complex geometries in small spaces, 3D-printing can be a solution. In this paper, a 3D-printed cold plate was designed and characterized with water coolant. The printed metal fin structures were strong enough to undergo pressure from the fluid flow even at high flow rates and small fin structures. A copper block with top surface area of 1 inch by 1 inch was used to mimic a computer chip. Experimental data has good match with a simulation model which was built using commercial software 6SigmaET. Effects of geometry parameters and operating parameters were investigated. Fin diameter was varied from 0.3 mm to 0.5 mm and fin height was maintained at 2 mm. A special manifold was designed to maximize the surface contact area between coolant and metal surface and therefore minimize thermal resistance. The flow rate was varied from 0.75 L/min to 2 L/min and coolant inlet temperature was varied from 25 to 48 °C. It was observed that for the coolant inlet temperature 25 °C and aluminum cold plate, the junction temperature was kept below 63.2 °C at input power 350 W and pressure drop did not exceed 23 Kpa. Effects of metal materials used in 3D-printing on the thermal performance of the cold plate were also studied in detail.

## 1. Introduction

Data centers recently face a challenge in the increase of power densities for high-power electronics. Recently, engineers and scientists are interested in heterogeneous integration that can enable higher performance, lower latency, smaller size, lighter weight, lower power requirement per function, and lower cost of electronics industry. In heterogeneous integration, the separately manufactured components are combined in the same package. The integrated components can vary in functionality, such as specialized processors, DRAM, flash memory, filters, connectors, and MEMS device. Heterogeneous leads to

significant challenges for thermal management such as heat extraction from hot spots, heat transfer through multiple layers of materials, and different target temperatures for specific devices/materials. With high heat fluxes in data center, the rack power density can go up to 25-35 kW/rack while the traditional air-cooling method can only dissipate power up to 10 kW/rack. With higher specific heat and latent heat compared to air cooling, liquid cooling can be an alternative solution that can help increase power density, reduce physical scale, improve reliability, and enhance energy efficiency in the data center.

Liquid cooling technology has received significant attention for decades. The higher power density challenge recently led to the re-emergence of this advanced technology as an alternative for air cooling. A study by IBM [1] shows that if cooled by 25 °C water, the hybrid server uses ~14% less power, leading to over 2 kW in power savings per rack of 40 servers compared to air cooling. A pumped liquid two-phase cooling method was investigated by Kulkarni et al. [2]. It was found that all cold plates in series can effectively have the same fluid inlet temperature, and hence all CPUs can run at the same case or junction temperature.

In comparison, single-phase cooling increases inlet temperature from one cold plate to the next one in series. To get the required cooling for the last CPU in series, one has to provide a much lower glycol/water inlet temperature to the first cold plate to compensate for the temperature rise. Sahini et al. [3] studied high ambient inlet temperatures effects on the performance of air vs liquid-cooled IT equipment. It was observed that the CPU temperatures show a difference of 20 °C for the same computational load for air vs. liquid cooled system. The air-cooled system becomes inefficient after 35 °C inlet air temperature. On the other hand, in liquid cooling, even at an inlet temperature of 45 °C, the CPU temperatures are lower, and the cooling system operates effectively with increased stress loading and inlet temperature. Ramakrishnan et al. [4] experimentally studied a cold plate used in cooling multi-chip server modules. In their work, it was stated that enhanced microchannel design performed better than conventional parallel microchannels design. In addition, their study also highlighted the effects of flow direction in the microchannels relative to the package on the thermal performance. The response surface method (RSM) is used to optimize the geometry of an impingement microchannel cold plate in [5]. The results show that hydraulic resistance can be reduced by 50% without a significant change in thermal resistance. Micro-pins that are directly attached to the chip and eliminate the need for thermal interface materials were studied in [6]. Results show that the outlet port position has a significant effect on hydraulic and thermal resistances. A 47% reduction in pressure drop was achieved by varying fin height without sacrificing the thermal performance.

Geometry optimization of heat sink has recently drawn attention since the heat sink geometry can affect thermal performance and pumping power. Many works have been done for fin geometry and manifold geometry optimization [7-18]. Three fin parameters (thickness, height, and gap) and three groove

parameters were optimized to reach minimum values for hydraulic and thermal resistances in [7]. Xia et al. [8] experimentally investigated performance of circular micro pin-fin, square micro pin-fin and diamond micro pin-fin heat sinks. It was observed that the diamond pin fin shows the best thermal performance following by circular and square pin fin. Although having good thermal performance, the diamond pin fin shows higher pressure drop. Circular pin fin shows the best performance in pressure drop. The genetic algorithm was used to optimize the performance of the microchannel heat sink in terms of the pumping power and Nusselt number [9]. Results show that optimum results are observed for higher channel width and lower channel height. Topology design and optimization of the microchannel heat sink were investigated considering four topologies: ternate veiny, lateral veiny, snowflake shape and spider netted [10]. The straight conventional microchannel and spider netted microchannel were 3D printed, and the experimental results show that the spider netted microchannel was better than the straight microchannel. The difference of the maximum heat source temperature reached 9.9 °C at a heat flux 100 W/cm<sup>2</sup>. A comparison in performance between microchannel and pin fin array heat sinks was presented in [11]. The results show that pin fin array heat sink has better thermal performance than the microchannel heat sink. If the channel width of the microchannel is too small, the coolant may not be able to impinge down to the base. It can result in low thermal performance even though the total surface contact area between the coolant and the copper microchannels is maximized. Cutting the channel into pin fin arrays can leave enough space for impingement of coolant down to the base and improve thermal performance considerably.

There are geometries impossible for traditional methods to produce. 3D printing allows the creation and manufacture of such complicated geometries. In addition, 3D printing is a cost-effective manufacturing process that does not require a large number of expensive machines or labor costs like CNC machining and injection molding. Wei et al. [19] designed and characterized a package level 3D printed multi-jet cooler with sub-mm microjets, applied to a 23×23mm<sup>2</sup> large die with almost 1000W power dissipation. The results show that cooling on the bare die outperforms the cooling on the lidded package by 35%. There is a significant impact on the coolant flow distribution. Compared to the reference design with one inlet and one outlet, introducing an additional distribution layer of multi-jet and outlets reduces the chip temperature gradient by a factor of 4. Azizi et al. [20,21] performed how the Sn3Ag4Ti alloy can robustly bond onto silicon via selective laser melting (SLM). By employing this technology, heat removal devices (e.g., vapor chamber evaporators, heat pipes, micro-channels) can be directly printed onto the electronic package without using thermal interface materials. This method can keep the current microprocessor about 10 °C cooler by eliminating two thermal interface materials. Gonzalez-Valle et al. [22] experimentally characterize hybrid water-cooled heat sinks for multi-core CPUs. The heat sinks were composed of a copper plate and 3-D printed shells containing flow channel manifolds; four hybrid designs with 16, 32, and 64 jets were 3-D printed. It was observed that the inclusion of pin fins on the impinging surface yielded a

negligible effect on the pressure drop, indicating that for the hybrid heat sinks, the major pressure losses are within the fractal inlet and outlet manifolds. The addition of fins on the impinging surface drastically decreased the average core temperatures, while the number of jets in the hybrid configurations played a secondary role.

3-D printing is renowned for creating highly complicated parts, with a resolution of up to 20 µm, extending its applicability to various research fields. There is a great potential for applications of 3D printing in manufacturing electronics cooling prototypes. However, in general, the number of publications in 3D printed heat sink is limited. This paper used selective laser melting (SLM) to fabricate an aluminum alloy (AlSi10Mg) cold plate. Both the aluminum part and the manifold were 3D printed in the lab. A commercial software 6SigmaET was used to design and optimize the performance of the cold plate before manufacturing. A bench level experimental test rig was built to study the cold plate's heat transfer and hydraulic performance, with operating and geometry parameters variations. While the results make it evident that, the high heat generating components can be kept at operable conditions using the 3D printed cold plate; a deeper insight at the outcomes could pave way for more complex geometries and energy efficient cold plate designs.

## 2. Experimental Setup

## 2.1 Cooling Loop and Mock Package

Configuration of a closed-loop flow system for the experiments was presented in Figure 1. The test rig is similar to the one utilized in our previous papers [11, 23]. Key components of the flow loop system are the pump, flow meter, thermocouples, pressure transducer, heat exchanger, and chiller. De-ionized water was pumped from the reservoir through the cooling loop. T-type thermocouples and absolute pressure sensors were used to measuring coolant temperature and pressure at the inlet and outlet of the cold plate. A differential pressure sensor was used to measure pressure drop through the cold plate. The flow rate of the liquid coolant entering the cold plate is calculated using a volumetric flow meter (Omega FTB 336D) with a range of 0.2-2 LPM. A chiller (Julabo LH40) and a plate liquid-liquid heat exchanger were used to control the coolant temperature inside the loop. A LABVIEW program was written to gather data from sensors. A mock package was designed containing a copper block, insulation, cartridge heaters and the cold plate. The details of mock package components are shown in Figure 2. Four cartridge heaters (Omega CIR-3020/120V) were inserted at the bottom of the copper block and each cartridge heater can dissipate maximum power up to 400 W. The cold plate was placed on the top of the copper block using a thermal interface material (TIM) with a thermal conductivity of 12.5 W/mK (Kryonaut Thermal Grease). The cold

plate was fixed onto the top surface of copper block by a holder of the frame. Weights were placed on the weight seat for maintaining pressure and constant interfacial thickness. To minimize heat losses to the environment, the whole mock package was wrapped around by insulation layers of fiberglass. Then a polystyrene box was used to contain the mock package.

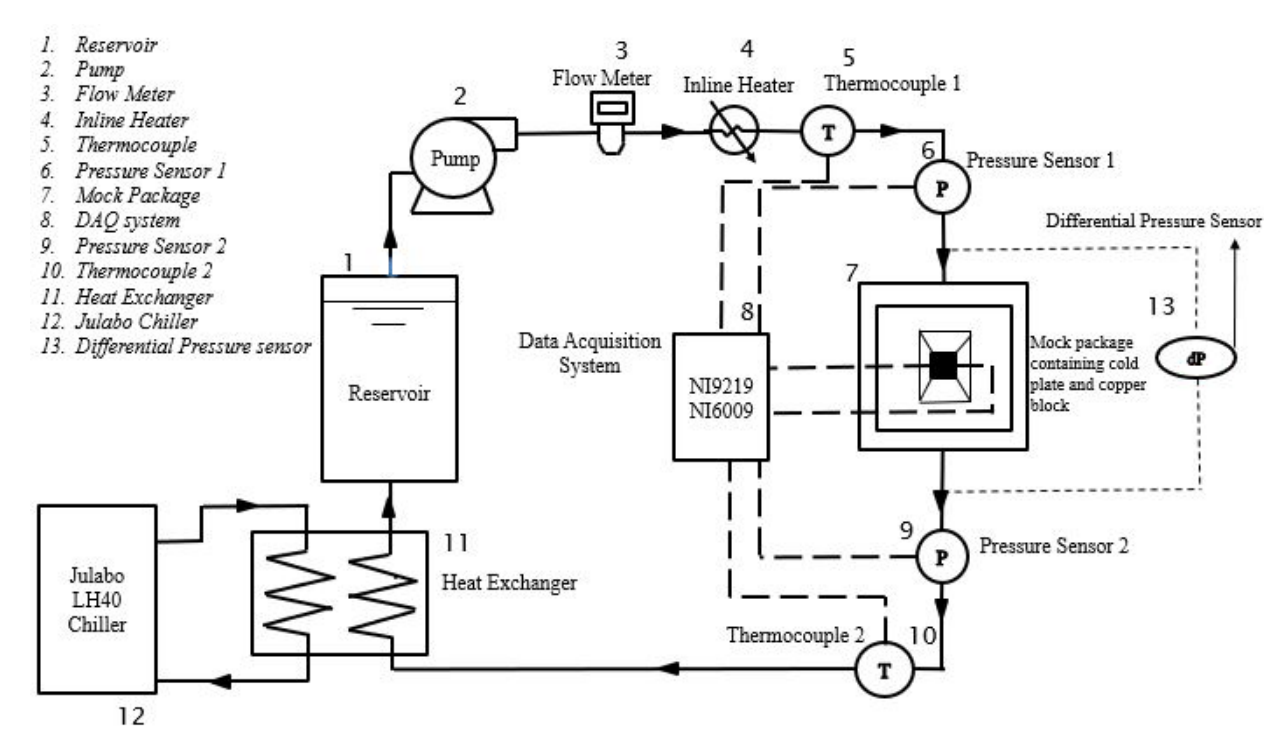


Figure 1. Schematic Diagram of the setup

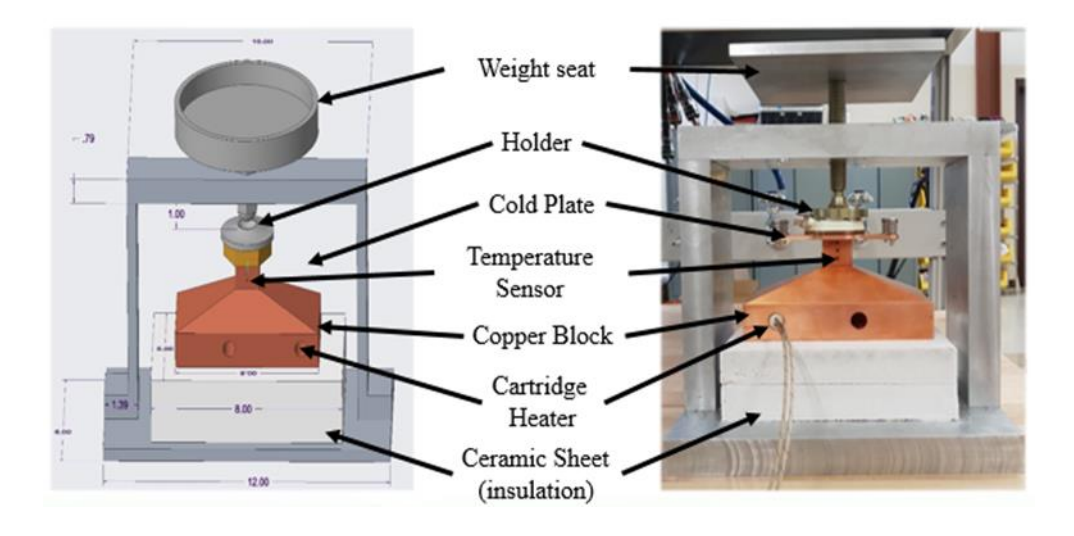


Figure 2. Components of the mock package

## 2.2 Cold plate design and manufacturing

Figures 3a and 3b show the schematic of the pin fin cold plate. The heat sink base has a thickness of 2 mm and an area of 45 mm x 45 mm. The fin part covers an area of 25.4 mm x 25.4 mm, which is the same as the mock chip area (copper block top surface). The manifold design was described in Figures 4a and 4b. The coolant impinges down from the manifold inlet, then spreads to the fins and leaves at the two outlet rectangle slits. The outlet slits are 20 mm in width and 1.5 mm in depth. The wider outlet slits can help in distribution of more uniform flow to the fins and base surface. The diameters of inlet tube and outlet tube are both 6.35 mm (1/4 inch).

The more uniform flow distribution can lead to a more uniform chip surface temperature. Before manufacturing the cold plate, a CFD model was built in the commercial software 6SigmaET to ensure the cold plate's thermal performance and pumping power are in a good range for a liquid cooling cold plate. Finally, the cold plate was 3D printed using selective laser melting (SLM). AlSi10Mg aluminum alloy with the thermal conductivity of 140 W/m-K was used as the material for 3D printing of the base and pin fins. Figure 5a shows the base and the pin fins after 3D printing process and the final cold plate, including the plastic manifold was demonstrated in Figure 5b. ABS plastic material was used for 3D printing of the manifold. Two T-type thermocouples were installed at the bottom of the cold plate to measure base temperature. Two grooves with dimension of 0.76 mm x 0.76 mm were machined to accommodate the thermocouples at the bottom of the heat sink base. The data acquisition system (NI-9219) was used to gather the temperature data from the thermocouples (T<sub>b</sub>). Three different fin diameters were manufactured to study the effects of pin fins geometry on the cold plate performance, including 0.3 mm, 0.4 mm, and 0.5 mm. The fin height of 2 mm was maintained constant for all 3D printed cold plates. Figure 6 shows the cold plates with fin diameters 0.3, 0.4 and 0.5 mm.

## 2.3 Experimental Procedure

The experiment was operated at a constant flow rate, a desired inlet coolant temperature, and zero mock chip power for about 30 minutes to remove trapped air inside the loop. The inlet coolant temperature was controlled by adjusting the liquid temperature in the chiller loop and the liquid-liquid heat exchanger. A constant flow rate was maintained by adjusting the supplied DC power to the pump. After 30 minutes of degassing at the coolant temperature higher than ambient temperature, a ventilation valve was used to vent the trapped air inside the reservoir. An AC power supply was used to power the four cartridge heaters. In every step of increasing power applied to the copper block, the flow rate was adjusted to ensure that a constant flow rate was maintained throughout the experiments. When the power of the mock chip increases, the coolant receives more sensible heat that leads to increase of coolant temperature and reducing of coolant

viscosity. The flow rate increases due to the reducing in viscosity and constant pressure from the pump. Therefore, the DC power to the pump needs to be adjusted to lower voltage for maintaining constant flow rate. In every step of input power, the author waits until the steady state of temperature and pressure before gathering data to an Excel file using the DAQ system and the LABVIEW program.



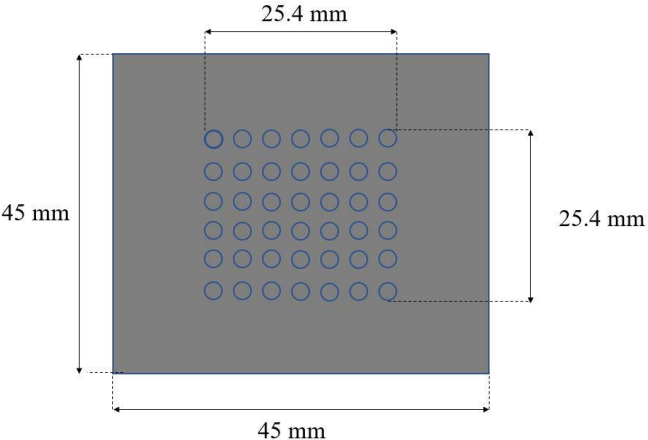


Figure 3a. Schematic showing base and pin fins of the cold plate

Figure 3b. Base and pin fins of the cold plate (top view)

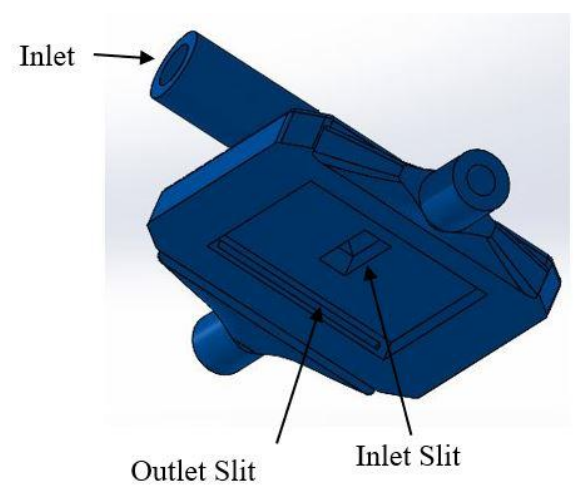


Figure 4a. Schematic of the manifold (bottom view)

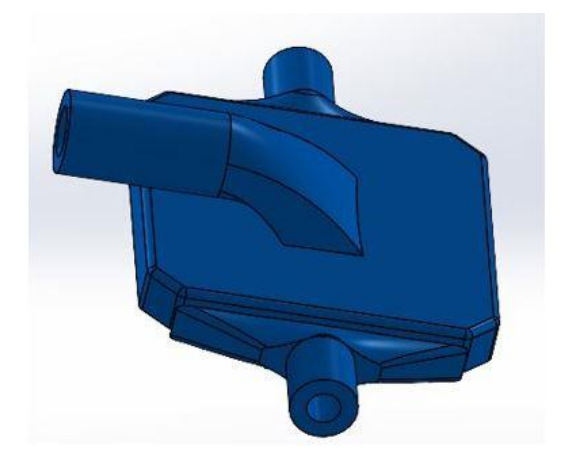


Figure 4b. Schematic of the manifold (top view)

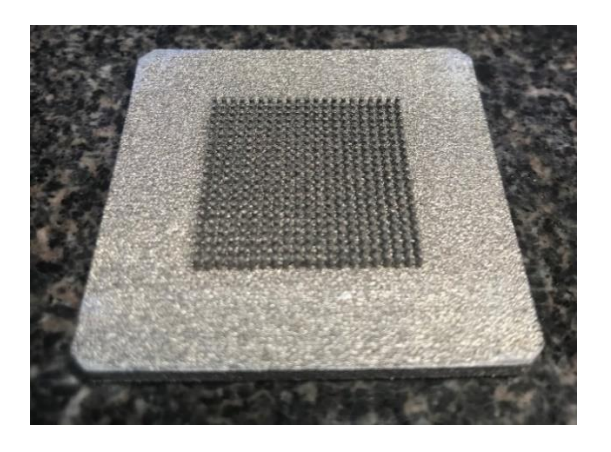


Figure 5a. 3D printed cold plate using selective laser melting (SLM)



Figure 5b. 3D printed cold plate including manifold



Figure 6. cold plates with fin diameters 0.3,0.4 and 0.5 mm

#### 3. Results and Discussion

## 3.1 Comparison between experimental and simulation data.

The thermal resistance results obtained by the numerical model are compared with the experimentally measured data in figure 7. For these results, the average and maximum discrepancies are less than 4.2% and 5.4%, respectively. The error analysis using root sum square method [23-26] for the experimental uncertainty in the thermal resistance for various heat fluxes was performed. The uncertainties of the thermal resistance generally decrease with heat flux. The uncertainty of thermal resistance is 12.5 % at heat flux 7.7 W/cm² and reaches the minimum of 2.5 % at a uniform heat flux of 63.6 W/cm². The uncertainty of pressure drop reduces with flow rate from 11.2 % at flow rate 0.75 L/min and has a minimum value of 3.4 % at flow rate 2 L/min. The commercial software 6SigmaET and finite volume method with K-epsilon model was

used to solve the governing equations numerically. Reynolds number was calculated by  $Re = \frac{\rho u d_n}{\mu}$ . Where  $d_n$  is the inlet jet diameter, u is the liquid velocity,  $\mu$  is the dynamic viscosity of the liquid, and  $\rho$  is the liquid density. Reynolds number has a range from 5634 to 15025. A grid sensitivity analysis was performed based on thermal resistance of heat sink. The number of cells was increased from 3 million to 18 million. The thermal resistance shows a variation less than 3% between 15 million and 18 million cells. Therefore, a grid with 15 million cells was selected for this geometry. It can be seen in Figure. 8 that there are at least 6 cells between the fins so that the turbulent flow in the channels can be captured by the model. The three-dimensional governing equations of mass, momentum, turbulent kinetic energy, turbulent energy dissipation rate, and energy in the steady turbulent main flow using the standard k-e model are given as follows:

Continuity equation:

$$\frac{\partial \rho u_i}{\partial x_i} = 0 \tag{1}$$

Momentum equation:

$$\rho u_j \frac{\partial u_i}{\partial x_j} = -\frac{\partial p}{\partial x_i} + \frac{\partial}{\partial x_j} \left[ \mu_t \left( \frac{\partial u_i}{\partial x_j} + \frac{\partial u_j}{\partial x_i} \right) \right] \tag{2}$$

Energy equation:

$$\rho u_j \frac{\partial T}{\partial x_j} = \frac{\partial}{\partial x_j} \left[ \left( \frac{\mu_l}{\sigma_l} + \frac{\mu_t}{\sigma_t} \right) \frac{\partial T}{\partial x_j} \right] \tag{3}$$

Transport equation for k:

$$\rho u_j \frac{\partial k}{\partial x_j} = \frac{\partial}{\partial x_j} \left( \frac{\mu_t}{\sigma_k} \frac{\partial k}{\partial x_j} \right) + \mu_t \left( \frac{\partial u_i}{\partial x_j} + \frac{\partial u_j}{\partial x_i} \right) \frac{\partial u_i}{\partial x_j} - \rho \varepsilon \tag{4}$$

Transport equation for  $\varepsilon$ :

$$\rho u_j \frac{\partial \varepsilon}{\partial x_j} = \frac{\partial}{\partial x_j} \left( \frac{\mu_t}{\sigma_{\varepsilon}} \frac{\partial \varepsilon}{\partial x_j} \right) + C_1 \mu_t \frac{\varepsilon}{k} \left( \frac{\partial u_i}{\partial x_j} + \frac{\partial u_j}{\partial x_i} \right) \frac{\partial u_i}{\partial x_j} - C_2 \rho \frac{\varepsilon^2}{k}$$
 (5)

Figure 9 shows the temperature map of the cold plate base in the case of  $T_{in} = 36$  °C, thermal design power 150 W, and flow rate 1 L/min. The temperature increases along the flow direction of the coolant due to the caloric thermal resistance. The temperature gradient on the top of the chip surface is small with maximum and minimum temperature values of 49.4 and 47.8 °C, respectively, which means the temperature gradient

is lower than 1.6 °C on the surface of the cold pate base. A smaller temperature gradient can improve the pacing, performance, and lifetime of the computer chip. The temperature gradient of the current cold plate is impressive and much better than many other water-cooled cold plates [29-31]. In addition to max temperature, the temperature gradient along the chip is also very important parameter. High temperature gradient can lead to electromigration and shorten lifetimes of electronics devices. The result in this section reveals that there is a good match between simulation and experimental data. In addition, this cold plate has good thermal performance which is promising for high heat flux applications. It can also be observed in Figure 9 that temperature is higher at the edge. The design of our setup allows us to measure the T<sub>junc</sub> at the center since we placed the thermocouples at the center of the copper block but not at the edge. This will be taken into account for the next designs and publications. We can place several thermocouples along the horizontal direction in order to obtain temperature distribution. The positions of the thermocouples can be chosen based on numerical modeling before we drill the holes for placing the thermocouples

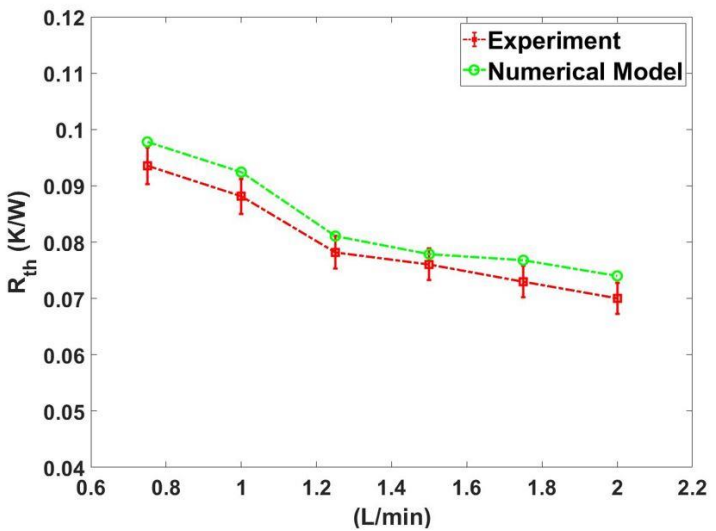


Figure 7. Comparison of numerical and experimental thermal resistance data at different flow rates/channel Reynolds numbers for the case of 0.3 fin diameter,  $T_{in} = 36$  °C.

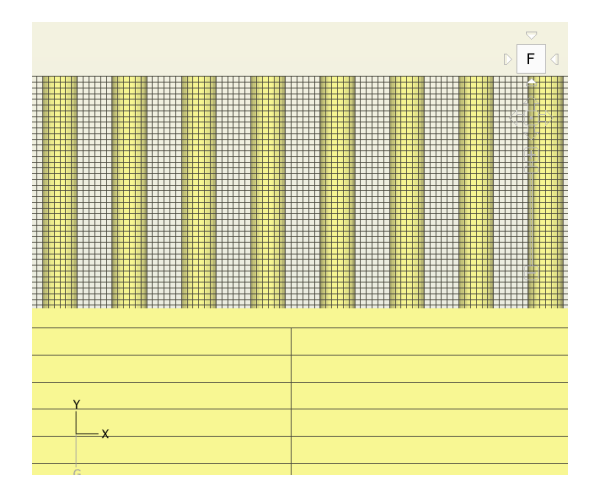


Figure 8. Meshing for fins and channels. Grid cells are hexahedral with greater concentration on channels.

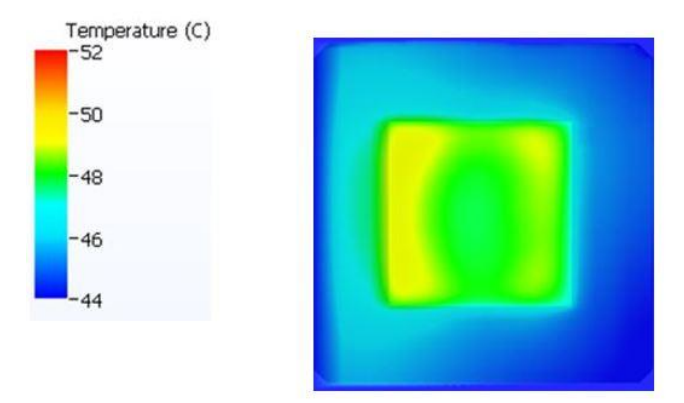


Figure 9. Temperature profile at the cold plate base,  $T_{in} = 36$  °C, thermal design power 150 W, and flow rate 1 L/min

# 3.2 Effects of fin geometry

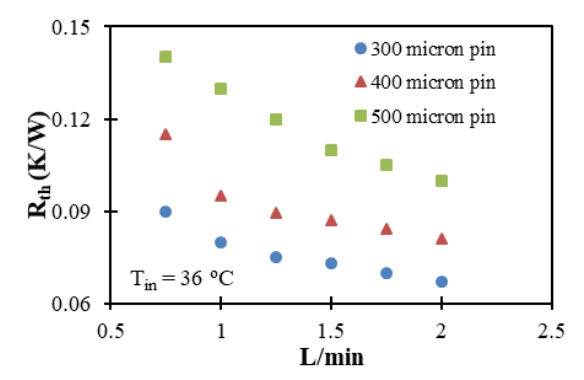
Variations of thermal resistance with flow rate at different fin diameters were presented in Figure 10a. Thermal resistance of the cold plate was calculated by the formula:

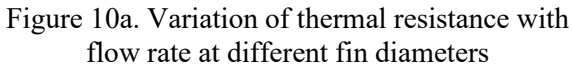
$$R_{th} = \frac{T_b - T_{in}}{O}$$

T<sub>b</sub> is the base temperature, T<sub>in</sub> is the coolant inlet temperature, and Q is the input power dissipated from the four cartridge heaters. The fin diameters of 300 microns, 400 microns, and 500 microns were studied. The fin pitch was the same as the fin diameters in all designs. With increasing of contact area between the coolant and the metal surface, the case of 300 microns pin shows the lowest thermal resistance of 0.064 K/W at the flow rate 2 L/min. This thermal resistance of 0.064 K/W is pretty good as compared to other liquid cooling aluminum heat sinks [27,28]. Li et al. [27] experimentally investigated aluminum foam heat

sinks through integrated pin fins with thermal resistance from 0.066 to 0.175 K/W. Chiu et al. [28] studied the liquid cooling efficiency of aluminum heat sinks containing micro pin fins with thermal resistance from 0.28 to 0.75 K/W and pressure drop from 0.7 to 2.8 kPa. It can be seen in Figures 10a and 10b that although thermal resistance decreases considerably with decreasing of fin diameter, the pressure drop does not change too much when fin diameter reduces from 500 microns to 300 microns. At the same flow rate of 2 L/min, pressure drops for fin diameter 500 microns and 300 microns are 21.1 and 28.1 kPa, respectively, while thermal resistance decreases by 39 % from 0.106 K/W to 0.064 K/W when fin diameter reduces from 500 microns to 300 microns.

3D printed heat sinks are very interesting topics for electronics cooling community. With 3D printing, we can design, and manufacture complex designs that conventional manufacturing methods cannot obtain. Figure 11 shows a complex design with half fat fin 0.4 mm and half small fin (0.3 mm). Figure 12 presents the comparison between the thermal performance of different fin geometries: uniform 0.4 mm, uniform 0.3 mm, and half 0.4 mm + half 0.3 mm. The case of 0.4 mm fin diameter has the highest base temperature following by the case of 0.3 mm diameter, and half 0.4 mm + half 0.3 mm. The fin pitch is maintained the same as the fin diameter. Therefore, the fin 0.3 mm shows significant higher thermal performance due to higher convection area as compared to the case of 0.4 mm fin. The highest thermal performance was obtained in the case of half 0.3 mm and half 0.4 mm with more uniform temperature distribution and lower base temperature. The higher thermal performance is attributed to the higher convection in the 0.3 mm area and more flow rate in the 0.4 mm area.





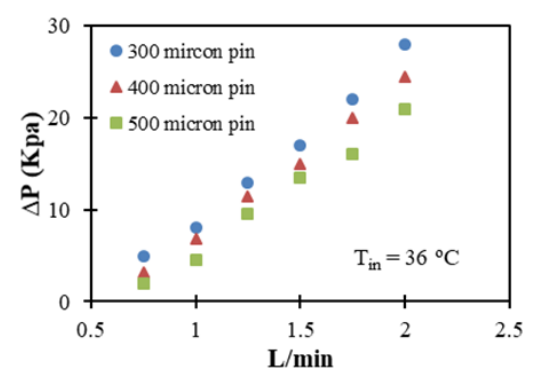


Figure 10b. Variation of pressure drop through the cold plate with flow rate at different fin diameters

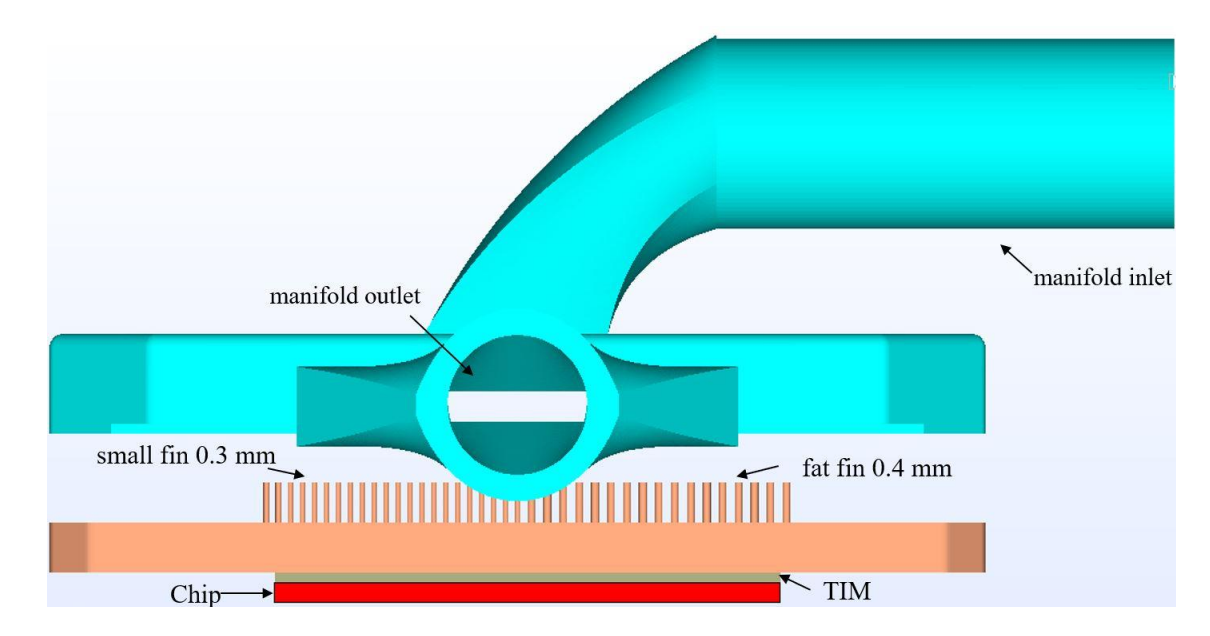


Figure 11. The design of a complex fin geometry with half fat fin (0.4 mm) and half small fin (0.3 mm)

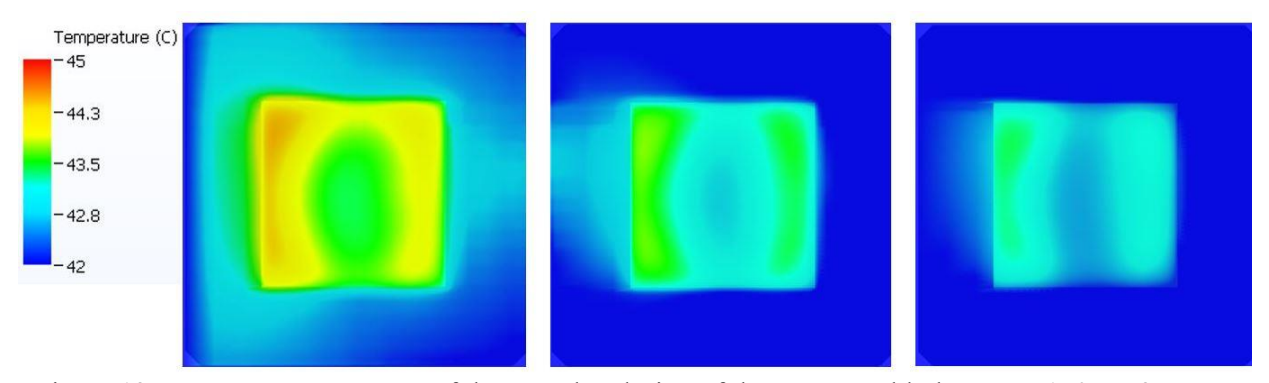


Figure 12. Base temperature map of the complex design of the copper cold plate: Q = 150 W, 2LPM,  $36 \,^{\circ}\text{C}$  inlet temperature. From left to right: fin 0.4 mm, fin 0.3 mm, half 0.4 and half 0.3 mm

# 3.3 Effects of operating parameters

Effects of operating parameters on thermal performance and pressure drop were also studied in detail. The measured cold plate resistance in equation (6) includes the convective resistance, the resistance from the conduction at the cold plate base, and the caloric resistance due to flow.

$$R_{th} = R_{convec} + R_{conduction} + R_{caloric}$$
 (6)

$$R_{convec} = \frac{1}{A_{hs}h_{hs}} \tag{7}$$

$$R_{caloric} = \frac{1}{m_c C_n} \tag{8}$$

$$R_{conduction} = \frac{t_b}{kL_{ch}W_{ch}} \tag{9}$$

Based on the analysis of these equations (6-9), variation of coolant inlet temperature or flow rate can lead to changes of convective resistance  $R_{convec}$  and caloric resistance  $R_{caloric}$ , which contribute to the variation in the total resistance  $R_{th}$ . The flow rate increases from 0.75 L/min to 2 L/min, and the coolant inlet temperature varies from 25 to 45 °C at the same chip power of 140 W. It can be seen in Figure 13a that the thermal resistance slightly decreases with coolant temperature. The decrease of thermal resistance with coolant inlet temperature is attributed to the increase in thermal conductivity and the coolant's specific heat with temperature range from room temperature to 100 °C. At the same flow rate of 2 L/min, the thermal resistances of the cases  $T_{in} = 36$  °C and  $T_{in} = 40$  °C were 0.087 K/W and 0.083 K/W, respectively. Pressure drop also decreases slightly with coolant temperature. It is observed in figure 13b that the decrease of viscosity with temperature causes a small reduction in pressure drop through the cold plate. At the same flow rate of 2 L/min, the pressure drops at T<sub>in</sub> = 36 °C and T<sub>in</sub> = 40 °C are 24.4 kPa and 23.5 kPa, respectively. This reduction in pressure drop can result in lower pumping power and more energy savings. Another advantage of higher coolant inlet temperature is the potential for waste heat recovery and energy efficiency. The variation of base temperature of the cold plate with flow rate and coolant inlet temperature is presented in Figure 14. The base temperature generally increases with coolant inlet temperature. Although thermal resistance decreases with coolant temperature, the change in thermal resistance is small. The change in coolant inlet temperature is more significant; therefore, the base temperature increases with increasing coolant inlet temperature. At the same flow rate of 2 L/min, the base temperature in the cases of  $T_{in} = 25$  °C and  $T_{in} = 45$  °C were  $T_b = 39.1$  °C and  $T_b = 58.5$  °C, respectively. The higher base temperature will lead to higher chip temperature, lower chip performance, and reliability. Therefore, there should be a compromise when we increase coolant inlet temperature to have good energy savings at an acceptable chip temperature in the data center.

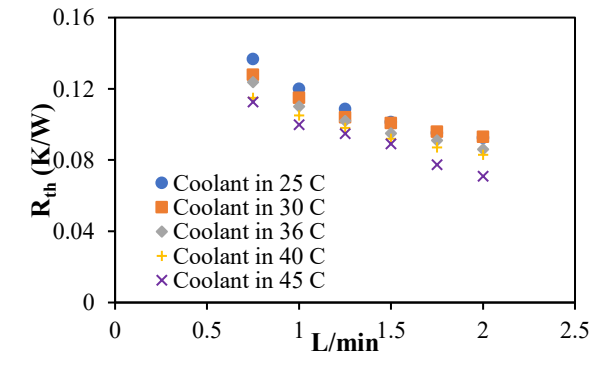


Figure 13a. Variation of thermal resistance with flow rate at different coolant inlet temperature, fin diameter 400 microns

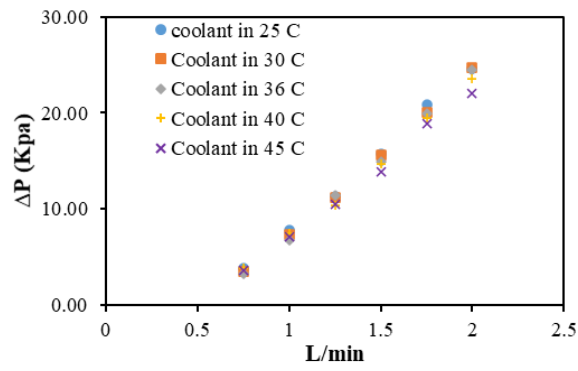


Figure 13b. Variation of pressure drop through the cold plate with flow rate at different coolant inlet temperature, fin diameter 400 microns

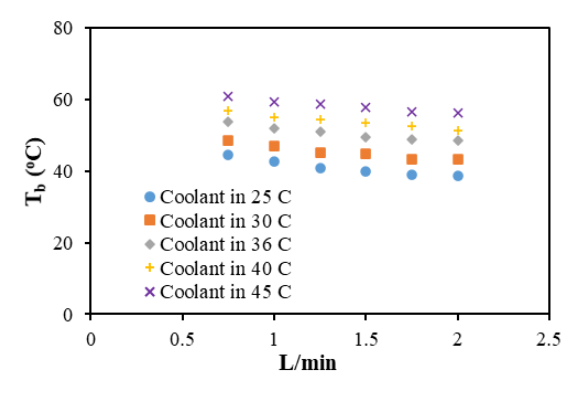


Figure 14. Variation of the base temperature of the cold plate with flow rate at different coolant inlet temperature, fin diameter 400 microns

## 3.4 Effects of materials

Effects of materials on the thermal performance of the cold plate was presented in Figure 15. Copper alloy, aluminum alloy, and silver alloy were the materials tested in this study. The thermal properties of each material were shown in table 1. It should be noticed that figure 15 presented the data from numerical model. Silver and aluminum alloys have lower melting point and more pliable than copper. These properties make silver and aluminum alloys more suitable for 3D printing than copper. However, we will manage to manufacture the 3D printed cold plate with copper material. It was shown in Figure 15 that the silver alloy cold plate has the best thermal performance thanks to the highest thermal conductivity of 423.9 W/mK at 20 °C. The thermal resistance of silver alloy cold plate can be as low as 0.037 K/W at the flow rate 2 L/min. With a thermal conductivity of 380.2 W/mK, the copper alloy cold plate has thermal resistance of 0.038 K/W at the flow rate 2 L/min. The aluminum alloy cold plate has significantly lower thermal performance than the copper and silver cold plate. With the thermal conductivity of 140 W/mK at 20 °C, the aluminum alloy cold plate has the thermal resistance of 0.068 K/W at the flow rate 2 L/min.

Table 1. Thermal properties of the materials used for the 3D printed cold plate.

| Reference<br>temperature (°C) | Material | Thermal<br>Conductivity<br>(W/mK) | Melting point (°C) | Density (g/cm³) |
|-------------------------------|----------|-----------------------------------|--------------------|-----------------|
| 20                            | Cu alloy | 380.2                             | 1095               | 8.89            |
| 20                            | AlSi10Mg | 140                               | 660.3              | 2.7             |
| 20                            | Ag alloy | 423.9                             | 970                | 10.5            |

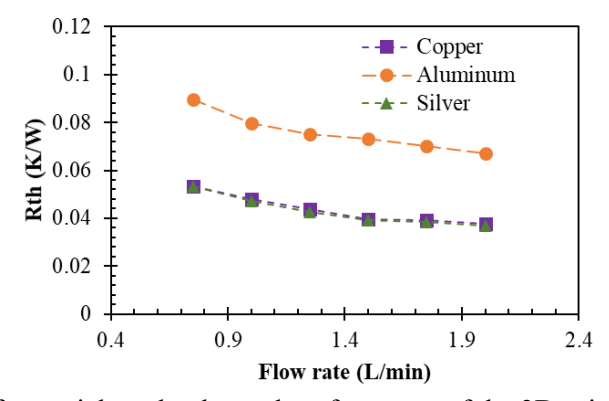


Figure 15. Effects of material on the thermal performance of the 3D printed cold plate. Copper, silver, and aluminum alloys were the materials studied in this work.

## 3.5 Junction Temperature

The Figure 16 shows junction temperature variation with flow rate when fin diameter increased from 300 microns to 500 microns and input power was maintained at 350 W. The maximum acceptable junction temperature of the CPU is 85 °C before thermal throttling occurs [35]. T<sub>junc</sub> max is the maximum temperature that a processor will allow prior to using internal thermal control mechanisms to reduce power and limit temperature. It can be observed in Figure 16 that the junction temperature was well below 85 °C at most of the points. Only in the case of fin diameter 500 microns, the junction temperature was 91.9 °C at a low flow rate of 0.75 L/min then reduced significantly with coolant flow rate until it reached 75.6 °C at flow rate 2 L/min. In the case of fin diameter 300 micron and flow rate 2 L/min, the junction temperature was 63.2 °C when input power 350 W was applied. Since the junction temperature is well below maximum value 85 °C, much higher input power for the case of 300 micro diameters + 2 L/min can be dissipated at an acceptable junction temperature. Figure 17 shows how the junction temperature was obtained in the current work. Three thermocouples T<sub>1</sub>, T<sub>2</sub>, T<sub>3</sub> were inserted to the copper block to measure heat flux through the copper top surface using Fourier law of heat conduction. T<sub>junc</sub> is the temperature obtained at the top surface of the copper block and calculated by using Fourier law to extrapolate from the thermocouple temperature  $T_1$ . The junction temperature can be calculated by the equation:  $T_{junc} = T_1 - \frac{Q\Delta x}{kA}$ . Where Q is the heat input,  $\Delta x$  is the distance between the thermocouple  $T_1$  and the mock chip surface  $T_{\text{junc}}$  k is the thermal conductivity of copper, and A is the chip surface area.

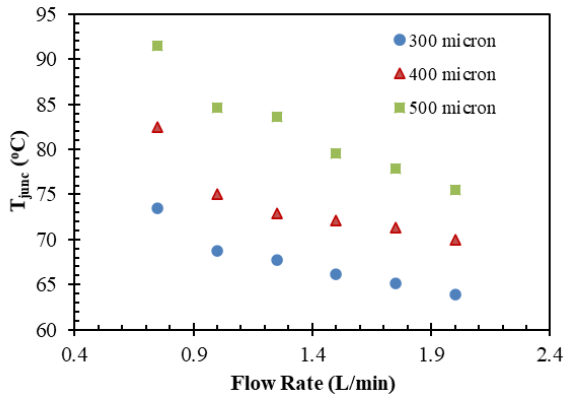


Figure 16. Variation of junction temperature with flow rate at different fin diameters,  $T_{in}$  =25 °C, input power 350 W

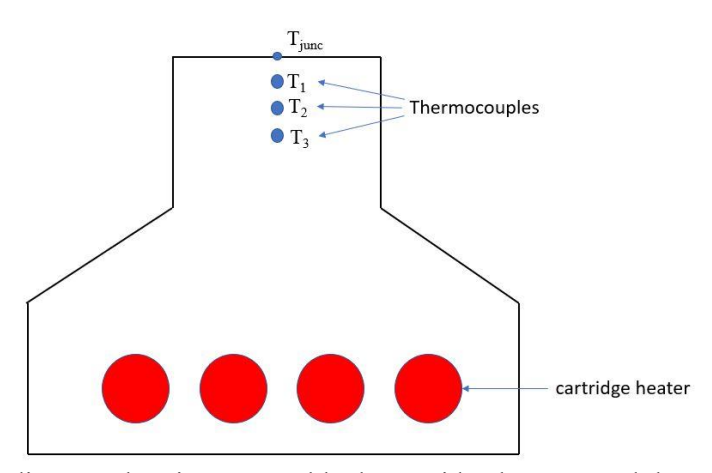


Figure 17. Schematic diagram showing copper block, cartridge heaters, and thermocouples

## 3.6 Comparison with state-of-the-art designs.

Table 2 compares thermal resistance and pressure drop of the copper alloy cold plate in the current study with the state-of-the-art studies. The CoolIT cold plate [34] has the lowest thermal resistance of 0.031 K/W. Another study from CoolIT [32] has thermal resistance of 0.051 K/W. A slightly higher thermal resistance of 0.053 K/W was obtained by Baidu [33]. The current study has thermal resistance of 0.048 K/W for copper alloy, which is pretty good as compared to the state-of-the-art works.

Table 2. Comparison of different copper alloy cold plates in industry at the same coolant flow rate 1 L/min.

| Author                        | $R_{th}$ (K/W) | $\Delta P (kPa)$ | Fin Geometry | Manifold<br>Geometry  |
|-------------------------------|----------------|------------------|--------------|-----------------------|
| Wagner [32] (CoolIT)          | 0.051          |                  | microchannel | Impingement           |
| Gao [33] (Baidu)              | 0.053          |                  | microchannel | Side in - side<br>out |
| Ramakrishnan [34]<br>(CoolIT) | 0.031          | 8.54             | microchannel | Impingement           |
| Current Study                 | 0.048          | 8.14             | pin fins     | Impingement           |

#### 4. Conclusion

In this study, an impingement 3D-printed micro pin-fin cold plate was designed and experimentally characterized. In addition, a numerical model was developed and validated using the experimental data. The sophisticated test setup was built to observe the performance of a novel cold plate using water as the working fluid under various operating and geometry conditions like flow rate, water inlet temperature, input power to the dies, pin fin diameter. Thanks to lower melting point, aluminum is an appropriate material used for the 3D printed cold plate. A minimum thermal resistance of 0.067 K/W was obtained for the case of aluminum cold plate at flow rate 2 L/min. The effects of material on the thermal performance of the cold plate was also studied in detail. Due to high thermal conductivity, the silver cold plate shows the best thermal performance with thermal resistance of 0.036 K/W following by copper cold plate (0.037 K/W) and aluminum cold plate at the same operating conditions of inlet temperature and flow rate. The additive manufacturing process successfully machined a fin diameter as small as 0.3 mm and could have been smaller if considering the best tips for 3D printing small objects.

The results in this paper reveal that when the 3D-printed cold plates are properly designed, they can support high heat flux in heterogeneous integration and enhance the energy efficiency of the HPC rack-level cooling system. The cold plates can be put together in series and parallel for operation in the rack level system. Due to the fact that, additive manufacturing gives developers maximum geometric design freedom, and complexity only plays a minor role in the production costs, future studies are planned to optimize the cold plate with a higher level of geometry complexity.

#### **ACKNOWLEDGEMENT**

This research is supported by the Semiconductor Research Corporation (SRC) through the Center for Heterogeneous Integration Research on Packaging (CHIRP) <a href="https://www.src.org/program/grc/chirp/">https://www.src.org/program/grc/chirp/</a>, Task 2878.

#### REFERENCE

 T. J. Chainer, M. D. Schultz, P. R. Parida and M. A. Gaynes, "Improving Data Center Energy Efficiency With Advanced Thermal Management," in *IEEE Transactions on Components, Packaging* and Manufacturing Technology, vol. 7, no. 8, pp. 1228-1239, Aug. 2017, doi: 10.1109/TCPMT.2017.2661700.

- 2. D. Kulkarni, X. Tang, S. Ahuja, R. Dischler, and R. Mahajan, "Experimental Study of Two-Phase Cooling to Enable Large-Scale System Computing Performance," 2018 17th IEEE Intersoc. Conf. Therm. Thermomechanical Phenom. Electron. Syst., pp. 596–601, 2018.
- M. Sahini, U. Chowdhury, A. Siddarth, T. Pradip, D. Agonafer, R. Zeigham, J. Metcalf, S. Branton,
  "Comparative study of high ambient inlet temperature effects on the performance of air vs. liquid cooled
  IT equipment," 2017 16th IEEE Intersociety Conference on Thermal and Thermomechanical
  Phenomena in Electronic Systems (ITherm), Orlando, FL, 2017, pp. 544-550, doi:
  10.1109/ITHERM.2017.7992534.
- 4. B. Ramakrishnan, Y. Hadad, S. Alkharabsheh, P. Chiarot, K. Ghose, B. Sammakia, V. Gektin, W. Chao "Experimental Characterization of Cold Plates used in Cooling Multi Chip Server Modules (MCM)," Proc. 17th Intersoc. Conf. Therm. Thermomechanical Phenom. Electron. Syst. ITherm 2018, no. Mcm, pp. 664–672, 2018, doi: 10.1109/ITHERM.2018.8419643.
- Y. Hadad, N. Fallahtafti, L. Choobineh, C. H. Hoang, V. Radmard, P. Chiarot, B. Sammakia, "Performance Analysis and Shape Optimization of an Impingement Microchannel Cold Plate," in *IEEE Transactions on Components, Packaging and Manufacturing Technology*, vol. 10, no. 8, pp. 1304-1319, Aug. 2020, doi: 10.1109/TCPMT.2020.3005824.
- V. Radmard, Y. Hadad, A. Azizi, S. Rangarajan, C. H. Hoang, C. Arvin, K. Sikka, S. Schiffres, B. Sammakia, "Direct Micro-Pin Jet Impingement Cooling for High Heat Flux Applications," 2020 36th Semiconductor Thermal Measurement, Modeling & Management Symposium (SEMI-THERM), San Jose, CA, USA, 2020, pp. 1-9, doi: 10.23919/SEMI-THERM50369.2020.9142864.
- 7. Y. Hadad, R. Pejman, B. Ramakrishnan, P. R. Chiarot and B. G. Sammakia, "Geometric Optimization of an Impinging Cold-Plate with a Trapezoidal Groove Used for Warm Water Cooling," 2018 17th IEEE Intersociety Conference on Thermal and Thermomechanical Phenomena in Electronic Systems (ITherm), San Diego, CA, USA, 2018, pp. 673-682, doi: 10.1109/ITHERM.2018.8419540.
- 8. G. Xia, Z. Chen, L. Cheng, D. Ma, Y. Zhai, and Y. Yang, "Micro-PIV visualization and numerical simulation of flow and heat transfer in three micro pin-fin heat sinks," Int. J. Therm. Sci., vol. 119, pp. 9–23, 2017, doi: https://doi.org/10.1016/j.ijthermalsci.2017.05.015.
- 9. Y. Alperen and C. Sertac, "Multi objective optimization of a micro-channel heat sink through genetic algorithm," *Int. J. Heat Mass Transf.*, vol. 146, p. 118847, 2020, doi: https://doi.org/10.1016/j.ijheatmasstransfer.2019.118847.
- 10. H. Tan, L. Wu, M. Wang, Z. Yang, and P. Du, "Heat transfer improvement in microchannel heat sink by topology design and optimization for high heat flux chip cooling," *Int. J. Heat Mass Transf.*, vol. 129, pp. 681–689, 2019, doi: <a href="https://doi.org/10.1016/j.ijheatmasstransfer.2018.09.092">https://doi.org/10.1016/j.ijheatmasstransfer.2018.09.092</a>.

- 11. C. H. Hoang, M. Tradat, Y. Manaserh, B. Ramakrisnan, S. Rangarajan, Y. Hadad, S. Schiffres, B. Sammakia, "Liquid Cooling Utilizing a Hybrid Microchannel/Multi-Jet Heat Sink: A Component Level Study of Commercial Product." Oct. 27, 2020, doi: 10.1115/IPACK2020-2627.
- 12. X. Shi, S. Li, Y. Mu, and B. Yin, "Geometry parameters optimization for a microchannel heat sink with secondary flow channel," *Int. Commun. Heat Mass Transf.*, vol. 104, pp. 89–100, 2019, doi: <a href="https://doi.org/10.1016/j.icheatmasstransfer.2019.03.009">https://doi.org/10.1016/j.icheatmasstransfer.2019.03.009</a>.
- 13. M. Khoshvaght-Aliabadi, S. Deldar, and S. M. Hassani, "Effects of pin-fins geometry and nanofluid on the performance of a pin-fin miniature heat sink (PFMHS)," *Int. J. Mech. Sci.*, vol. 148, pp. 442–458, 2018, doi: <a href="https://doi.org/10.1016/j.ijmecsci.2018.09.019">https://doi.org/10.1016/j.ijmecsci.2018.09.019</a>.
- 14. Y. Zhai, Z. Li, H. Wang, and J. Xu, "Thermodynamic analysis of the effect of channel geometry on heat transfer in double-layered microchannel heat sinks," *Energy Convers. Manag.*, vol. 143, pp. 431–439, 2017, doi: https://doi.org/10.1016/j.enconman.2017.04.013.
- 15. H. M. Ali and W. Arshad, "Effect of channel angle of pin-fin heat sink on heat transfer performance using water based graphene nanoplatelets nanofluids," *Int. J. Heat Mass Transf.*, vol. 106, pp. 465–472, 2017, doi: <a href="https://doi.org/10.1016/j.ijheatmasstransfer.2016.08.061">https://doi.org/10.1016/j.ijheatmasstransfer.2016.08.061</a>.
- 16. Z. Soleymani, M. Rahimi, M. Gorzin, and Y. Pahamli, "Performance analysis of hotspot using geometrical and operational parameters of a microchannel pin-fin hybrid heat sink," *Int. J. Heat Mass Transf.*, vol. 159, p. 120141, 2020, doi: https://doi.org/10.1016/j.ijheatmasstransfer.2020.120141.
- 17. E. Rasouli, C. Naderi, and V. Narayanan, "Pitch and aspect ratio effects on single-phase heat transfer through microscale pin fin heat sinks," *Int. J. Heat Mass Transf.*, vol. 118, pp. 416–428, 2018, doi: https://doi.org/10.1016/j.ijheatmasstransfer.2017.10.105.
- V. Radmard, Y. Hadad, S. Rangarajan, C. H. Hoang, N. Fallahtafti, C. L. Arvin, K. Sikka, S. N. Schiffres, & B. G. Sammakia, (2021), "multi-objective optimization of a chip-attached micro pin fin liquid cooling system," *Applied Thermal Engineering*, 195. https://doi.org/10.1016/j.applthermaleng.2021.117187
- 19. T. W. Wei, H. Oprins, V. Cherman, Z. Yang, Z. Yang, G. Van der Plas, B. Pawlak, L. England, E. Beyne, M. Baelmans, "Experimental and Numerical Study of 3D Printed Direct Jet Impingement Cooling for High Power, Large Die Size Applications," *IEEE Trans. Components, Packag. Manuf. Technol.*, pp. 1–10, 2020, doi: 10.1109/TCPMT.2020.3045113.
- 20. A. Azizi, M. A. Daeumer, and S. N. Schiffres, "Additive laser metal deposition onto silicon," *Addit. Manuf.*, vol. 25, no. August 2018, pp. 390–398, 2019, doi: 10.1016/j.addma.2018.09.027.
- A. Azizi, M. A. Daeumer, J. C. Simmons, B. G. Sammakia, B. T. Murray, and S. N. Schiffres, "Additive laser metal deposition onto silicon for enhanced microelectronics cooling," *Proc. Electron. Components Technol. Conf.*, vol. 2019-May, pp. 1970–1976, 2019, doi: 10.1109/ECTC.2019.00302.

- 22. C. U. Gonzalez-Valle, S. Samir, and B. Ramos-Alvarado, "Experimental investigation of the cooling performance of 3-D printed hybrid water-cooled heat sinks," *Appl. Therm. Eng.*, vol. 168, p. 114823, 2020, doi: https://doi.org/10.1016/j.applthermaleng.2019.114823.
- 23. C. H. Hoang, S. Rangarajan, S. Khalili, B. Ramakrisnan, V. Radmard, Y. Hadad, S. Schiffres, B. Sammakia, "Hybrid microchannel/multi-jet two-phase heat sink: A benchmark and geometry optimization study of commercial product," *Int. J. Heat Mass Transf.*, vol. 169, 2021, doi: 10.1016/j.ijheatmasstransfer.2021.120920.
- 24. R. J. Moffat, "Describing the uncertainties in experimental results," *Exp. Therm. Fluid Sci.*, vol. 1, no. 1, pp. 3–17, 1988, doi: <a href="https://doi.org/10.1016/0894-1777(88)90043-X">https://doi.org/10.1016/0894-1777(88)90043-X</a>.
- 25. B. Ramakrishnan, C. H. Hoang, S. Khalili, Y. Hadad, S. Rangarajan, A. Pattamatta, B. Sammakia, "Experimental Characterization of Two-Phase Cold Plates Intended for High-Density Data Center Servers Using a Dielectric Fluid," *J. Electron. Packag.*, vol. 143, no. 2, Mar. 2021, doi: 10.1115/1.4049928.
- C. H. Hoang, N. Fallahtafti, S. Rangarajan, A. Gharaibeh, Y. Hadad, C. Arvin, K. Sikka, S. Schiffres, B. Sammakia, "Impact of fin geometry and surface roughness on performance of an impingement two-phase cooling heat sink," *Appl. Therm. Eng.*, vol. 198, p. 117453, 2021, doi: https://doi.org/10.1016/j.applthermaleng.2021.117453.
- 27. Y. Li, L. Gong, M. Xu, and Y. Joshi, "Enhancing the performance of aluminum foam heat sinks through integrated pin fins," *Int. J. Heat Mass Transf.*, vol. 151, 2020, doi: 10.1016/j.ijheatmasstransfer.2020.119376.
- 28. H. C. Chiu, R. H. Hsieh, K. Wang, J. H. Jang, and C. R. Yu, "The heat transfer characteristics of liquid cooling heat sink with micro pin fins," *Int. Commun. Heat Mass Transf.*, vol. 86, no. June, pp. 174–180, 2017, doi: 10.1016/j.icheatmasstransfer.2017.05.027.
- 29. S. Panchal, R. Khasow, I. Dincer, M. Agelin-Chaab, R. Fraser, and M. Fowler, "Thermal design and simulation of mini-channel cold plate for water cooled large sized prismatic lithium-ion battery," *Appl. Therm. Eng.*, vol. 122, pp. 80–90, 2017, doi: <a href="https://doi.org/10.1016/j.applthermaleng.2017.05.010">https://doi.org/10.1016/j.applthermaleng.2017.05.010</a>.
- 30. S. Wiriyasart and P. Naphon, "Liquid impingement cooling of cold plate heat sink with different fin configurations: High heat flux applications," *Int. J. Heat Mass Transf.*, vol. 140, pp. 281–292, 2019, doi: https://doi.org/10.1016/j.ijheatmasstransfer.2019.06.020.
- 31. T. Acikalin and C. Schroeder, "Direct liquid cooling of bare die packages using a microchannel cold plate," in *Fourteenth Intersociety Conference on Thermal and Thermomechanical Phenomena in Electronic Systems (ITherm)*, 2014, pp. 673–679, doi: 10.1109/ITHERM.2014.6892346.

- 32. G. R. Wagner et al., "Test results from the comparison of three liquid cooling methods for high-power processors," 2016 15th IEEE Intersociety Conference on Thermal and Thermomechanical Phenomena in Electronic Systems (ITherm), 2016, pp. 619-624, doi: 10.1109/ITHERM.2016.7517605.
- 33. Gao, Tianyi, Shuai Shao, Yan Cui, Bryan Espíritu, Charles Ingalz, Hu Tang and Ali Heydari. "A study of direct liquid cooling for high-density chips and accelerators." 2017 16th IEEE Intersociety Conference on Thermal and Thermomechanical Phenomena in Electronic Systems (ITherm) (2017): 565-573.
- 34. Ramakrishnan, B., Hadad, Y., Alkharabsheh, S., Chiarot, P. R., and Sammakia, B. (July 12, 2019). "Thermal Analysis of Cold Plate for Direct Liquid Cooling of High Performance Servers." ASME. *J. Electron. Packag.* December 2019; 141(4): 041005. https://doi.org/10.1115/1.4044130
- 35. N. Lamaison, J. B. Marcinichen, J. R. Thome, (July 24, 2013). "Two-Phase Flow Control of Electronics Cooling With Pseudo-CPUs in Parallel Flow Circuits: Dynamic Modeling and Experimental Evaluation." *ASME. J. Electron. Packag*. September 2013; 135(3): 030908. https://doi.org/10.1115/1.4024590